Inorganic Chemistry
Article
pubs.acs.org/IC

Elucidating Band-Selective Sensitization in Iron(II) Polypyridine-TiO_2 Assemblies

David N. Bowman, James H. Blew, Takashi Tsuchiya, and Elena Jakubikova*

Department of Chemistry, North Carolina State University, Raleigh, North Carolina 27695, United States

Ⓢ *Supporting Information*

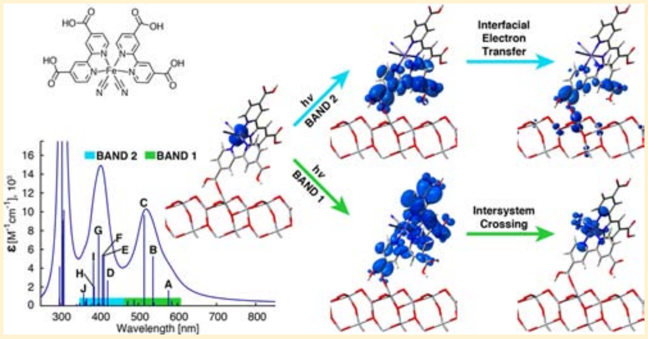

ABSTRACT: Iron(II) polypyridines represent a cheaper and nontoxic alternative to analogous Ru(II) polypyridine dyes successfully used as photosensitizers in dye-sensitized solar cells (DSSCs). We employ density functional theory (DFT) and time-dependent DFT (TD-DFT) to study ground and excited state properties of $[Fe(bpy)(CN)_4]^{2-}$, $[Fe(bpy\text{-}dca)(CN)_4]^{2-}$, and $[Fe(bpy\text{-}dca)_2(CN)_2]$ complexes, where bpy = 2,2′-bipyridine and dca = 4,4′-dicarboxylic acid. Quantum dynamics simulations are further used to investigate the interfacial electron transfer (IET) between the excited Fe(II) dyes and a TiO_2 nanoparticle. All three dyes investigated display two bands in the visible region of the absorption spectrum, with the major transitions corresponding to the metal-to-ligand charge transfer states. The calculated IET rates from the particle states created by the excitation of the lower-energy absorption band are comparable to or slower than the rate of the excited state decay into the nonemissive, metal-centered states of the Fe(II) dyes (~100 fs), indicating that the IET upon the excitation of this band is unlikely. Several particle states in the higher-energy absorption band display IET rates at or below 100 fs, suggesting the possibility of the IET between the Fe(II)-sensitizer and TiO_2 nanoparticle upon excitation with visible light. Our results are consistent with the previous experimental work on Fe(II) sensitizers (Ferrere, S. *Chem. Mater.* **2000**, *12*, 1083) and elucidate the band-selective nature of the IET in these compounds.

1. INTRODUCTION

Photoactive dyes anchored to wide band gap semiconductors are often utilized in assemblies for solar energy conversion, such as dye-sensitized solar cells (DSSCs)[1−4] or photocatalytic systems.[5−7] Although the current record efficiency in DSSCs is held by a Zn porphyrin dye,[8] some of the most efficient dyes are based on Ru(II) polypyridines.[9−11] Because of the high cost and toxicity of Ru, Fe(II) polypyridines have been evaluated previously as possible nontoxic and earth-abundant alternatives to Ru-based dyes.[12−19]

The ability of Fe(II) polypyridines to serve as photosensitizers in DSSCs was first demonstrated by Ferrere and Gregg, although their efficiency is much lower than that of their Ru analogues.[14] While they initially absorb visible light into similar metal-to-ligand charge-transfer (MLCT) states as Ru(II)-polypyridines, the photoactive MLCT states undergo intersystem crossing (ISC) into the low-lying high-spin metal-centered (MC) states on a subpicosecond time scale.[18] Therefore, the interfacial electron transfer (IET) between the excited dye and semiconductor occurs only from the initially populated "hot" MLCT states. Since the lifetime of the MLCT manifold of these systems is approximately 100 fs,[18,20,21] the IET must occur with a characteristic time of approximately 100 fs or less to be competitive with the ultrafast ISC events.

The work of Ferrere and Gregg also established the band-selective behavior of the IET between the short-lived excited MLCT states of $Fe(bpy\text{-}dca)_2(CN)_2$ (bpy-dca = 2,2′-bipyridine-4,4′-dicarboxylic acid) and TiO_2 semiconductor.[14] Ferrere et al. observed that upon the initial excitation with visible light, the IET is more efficient (10−11%) from the higher energy MLCT band and much less efficient (2%), from the lower energy MLCT transitions.

The goal of this work is to study the light absorption and IET processes for three different dye-TiO_2 nanoparticle systems, with a special focus on elucidating the origin of the band-selective IET in Fe(II) polypyridine-TiO_2 assemblies. The dyes investigated include $[Fe(bpy)(CN)_4]^{2-}$ (**1**), $[Fe(bpy\text{-}dca)(CN)_4]^{2-}$ (**2**), and $[Fe(bpy\text{-}dca)_2(CN)_2]$ (**3**), shown in Figure 1. Two of these dyes were studied previously, **1** by Meyer[15,16] and **3** Ferrere.[12,14] While **3** attaches to the TiO_2 surface via the carboxylic acid anchoring group, **1** is attached via the CN^--Ti bridge. Although dye **2** was not studied experimentally, it represents a natural bridge between the complexes **1** and **3** and was therefore included in our computational study.

Received: March 29, 2013
Published: July 9, 2013

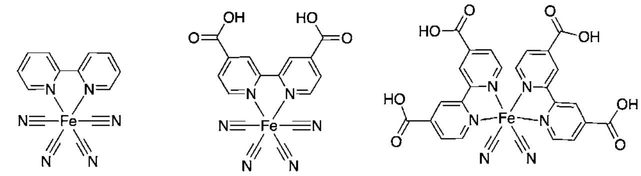

$[Fe(bpy)(CN)_4]^{2-}$ **1** $[Fe(bpy\text{-}dca)(CN)_4]^{2-}$ **2** $[Fe(bpy\text{-}dca)_2(CN)_2]$ **3**

Figure 1. Fe(II) complexes investigated in this work.

2. METHODS

2.1. Molecular Structure and Absorption Spectra. Dye molecules were optimized at the B3LYP[22,23] level of theory. The B3LYP functional was chosen for all calculations on Fe(II) polypyridine dyes as it provides good structural parameters[24] as well as reliable absorption spectra.[25] The SDD relativistic effective core potential (ECP) and associated basis set[26] were used to describe the central iron atom, and 6-31G* basis sets[27,28] were used for all other atoms. All complexes were optimized in the singlet ground state in vacuum. The calculation of UV−vis absorption spectra for dyes **1**−**3** was performed employing TD-DFT[29−31] methodology with the same basis set and functional as used for the geometry optimizations. Only spin allowed singlet vertical excitations were determined, and TD-DFT was performed on the entirely relaxed dye molecules **1**−**3**. Polarizable continuum model (PCM),[32] using acetonitrile as a solvent, was employed in the TD-DFT calculations. Absorption spectra were simulated by convoluting the stick spectrum composed of the δ-functions associated with each excitation energy times the oscillator strength with a Lorentzian line shape with half-width-at-half-maximum (HWHM) of 0.12 eV. Canonical Kohn−Sham orbitals were used to characterize absorption peaks with $f_{osc} > 0.01$, within the visible portion of the spectra ($\lambda > 350$ nm). The Gaussian 09 software package[33] was used for all the DFT and TD-DFT calculations on dye molecules.

2.2. Slab Model Optimization. The Vienna Ab-initio Simulation Package (VASP)[34−37] was used to optimize periodic systems (bulk TiO_2 and nanoparticles) at the DFT level of theory. The Perdew−Burke−Ernzerhof (PBE)[38,39] exchange-correlation functional with the Projector Augmented-Wave method[40,41] was employed in all periodic boundary calculations (PBCs). The PBE functional was chosen over B3LYP because of the computational efficiency considerations. Note that structure optimizations employing PBE and B3LYP functionals tend to result in nearly identical Ti−O and Ti−C bond lengths.[42] The plane wave basis set expansion was cut off at 500 eV for all PBCs. The unit cell for anatase TiO_2 was obtained with a (13 × 13 × 13) k-point sampling, resulting in a tetragonal lattice with lattice vectors $a = b = 3.81$ Å, $c = 9.77$ Å). The optimized geometry of the TiO_2 unit cell was used to construct a slab model of the (101) TiO_2 surface functionalized with either hydrogen cyanide or pyridine-4-carboxylic acid. The linker models and the top 2 layers of Ti and top 4 layers of O were relaxed using a (5 × 3 × 1) k-point sampling, keeping the supercell volume fixed with lattice vectors $a = 15.25$ Å, $b = 10.49$ Å, $c = 26.00$ Å. The bottom layers of the slab were fixed at bulk geometry.

The final model dye-nanoparticle assemblies were constructed by performing a constrained optimization of the dyes **1**−**3** with the linker groups (cyanide, and carboxylic acid in both monodentate and bidentate surface binding modes) fixed at surface-optimized geometries. Coordinates for the carboxylate functional group as well as the three closest carbons in the pyridine ring along with the two adjacent hydrogens were held frozen in the constrained optimization of dyes **2** and **3**. The Gaussian 09 software package,[33] employing the same functional and basis sets as described in section 2.1., was used for these constrained optimizations of dye with frozen linker geometry. Dyes **2** and **3** were attached to the slab surface in a cyanide, monodentate carboxylic acid, and bidentate carboxylate binding modes via the Kabsch alignment.[43] The Kabsch algorithm computes the optimal translation and rotation of a set of vectors (atomic positions of the dye) onto a corresponding set of reference vectors (atomic positions of the linker on top of the surface). Dye **1** was attached in the same manner with a cyanide binding mode. All the nonequivalent linker positions on the dyes were modeled: two nonequivalent carboxylic acid groups on **1** and **2** and two nonequivalent cyanide groups on **3**. All optimizations were performed in vacuum.

2.3. IET Simulations. All model systems were composed of a (101) anatase nanoparticle slab with dyes (**1**−**3**) attached via an anchoring group (cyanide or carboxylic acid) in vacuum, and their construction is described above. Quantum dynamics simulations to model the IET were performed on each dye-semiconductor model using a method developed by Rego and Batista,[44−48] employing the extended Hückel (EH) Hamiltonian. The description of the methodology presented below follows the one given by Rego and Batista.[44]

The initial particle (or excited) state is modeled as it undergoes time evolution with nuclear coordinates of the entire slab fixed. First a generalized eigenvalue problem is solved:

$$\mathbf{HQ^q} = \mathbf{E^qSQ^q} \tag{1}$$

where **H** is the EH matrix and **S** is the overlap matrix calculated in terms of the atomic orbital basis set. The initial state, $|\phi(0)\rangle$, is then expanded in terms of the orthonormal set of eigenvectors $|q\rangle$,

$$|\phi(0)\rangle = \sum_q C_q|q\rangle \tag{2}$$

and evolved in time

$$|\phi(t)\rangle = \sum_{i,\alpha} B_{i,\alpha}(t)|i,\ \alpha\rangle \tag{3}$$

In the above, $|i,\alpha\rangle$ denotes the atomic orbital α of atom i, $|q\rangle$ is defined as

$$|q\rangle = \sum_{i,\alpha} Q_{i,\alpha}{}^{q}|i,\ \alpha\rangle \tag{4}$$

and the time dependent expansion coefficients $B_{i,\alpha}(t)$ are calculated according to

$$B_{i,\alpha}(t) = \sum_q Q_{i,\alpha}{}^{q} C_q e^{-\left(\frac{i}{\hbar}\right)E_q t} \tag{5}$$

The value of interest for these simulations is the survival probability, $P(t)$, which is a fractional percentage of the total electron density that remains on the dye at a given simulation time. The survival probability is obtained at each simulation step by projecting the time-evolved wave function onto the atomic orbitals of the adsorbed chromophore:

$$P(t) = |\sum_{i\alpha}^{MOL} \sum_{j,\beta} B_{i,\alpha}{}^{*}(t) B_{j,\beta}(t) S_{\alpha,\beta}^{i,j}| \tag{6}$$

where $S_{\alpha,\beta}^{i,j} = \langle i,\alpha|j,\beta\rangle$. The indices α and β refer to specific orbitals in atoms i and j, respectively. The sum over MOL only applies to atoms in the initially excited dye.

For each system, donor states in the IET simulations were chosen from the particle states that make up major contributions to prominent excitations in the visible region of the absorption spectrum ($f_{osc} > 0.01$, $\lambda > 350$ nm) as calculated by TD-DFT calculations. The canonical Kohn−Sham (KS) orbitals corresponding to the relevant particle states were matched to the EH orbitals by visual inspection, which is straightforward for these systems. An example of two sets of matched orbitals for dye **3** is shown in Figure 2; see Figures S5, S7, and S10−S21 in the Supporting Information for more detailed information.

Simulations were run with a time step of 0.1 fs up to 3000 fs on supercell arrays with 30.49 Å × 31.46 Å × 26.00 Å dimensions. One k-point was used for sampling, and the calculations were run using periodic boundary conditions. All simulations were done at the frozen geometry. Absorbing potentials (i.e., imaginary terms to the diagonal elements of the Hamiltonian) were placed on the bottom layer of Ti atoms to avoid artificial recurrences in the electron-transient populations.

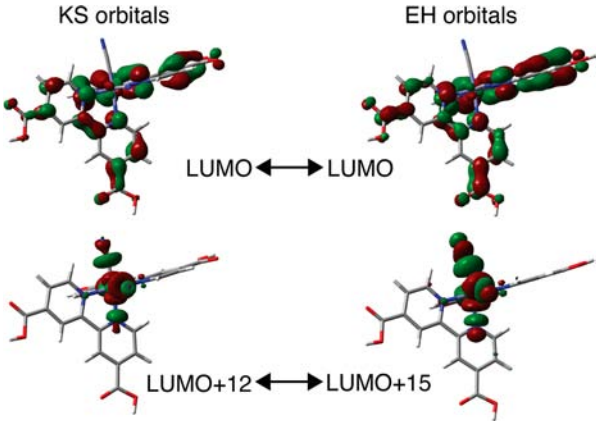

Figure 2. Example of matched orbitals for dye **3**. Kohn−Sham particle states LUMO and LUMO+12 are matched to EH orbitals LUMO and LUMO+15, respectively.

Characteristic electron injection times were obtained from an exponential fit of the survival probability defined by eq 6. The survival probability curves were fit with either an exponential decay function, or in the case that $R^2 < 0.95$, a biexponential decay function. The survival probability was constrained to unity at time 0 for all fits. The characteristic injection time was determined by the reciprocal of the decay constant for single exponential functions, or the reciprocal of the decay constant responsible for the majority of decay (coefficient >0.50) for the biexponential functions.

3. RESULTS AND DISCUSSION

The results are organized as follows: First the ground state molecular properties and absorption spectra are described for all dyes, followed by the description of the dye-nanoparticle assemblies. Finally, results of the IET simulation are summarized for each dye individually.

3.1. Ground State Structures and Absorption Spectra.

The optimized structures of dyes **1**−**3** are shown in Figure 3. Metal−ligand bond lengths for all three complexes are reported in Table 1, using the atom-numbering scheme from Figure 3. For dye **1**, we find a 2% error when comparing B3LYP metal−ligand bond length to the experimental crystal structure data.[49] For dye **2**, crystal structure data is unavailable, but we assume errors are similar to the related dye **1**. For dye **3**, crystal structure data is only available for the related species [Fe(bpy)$_2$(CN)$_2$]. When comparing the metal−ligand bond lengths for the singlet state of dye **3** to the corresponding bonds from the crystal structure of [Fe(bpy)$_2$(CN)$_2$], we find only a 2% error.[50] Overall, B3LYP provides accurate geometries for all the dyes.

Table 1. Metal Ligand Bond Lengths for the Complexes Investigated[a]

iron-ligand bond	bond lengths (Å) 1	2	3
Fe-L1 (CN$^-$)	1.959	1.955	1.942
Fe-L2 (CN$^-$)	1.988	1.977	1.942
Fe-L3 (CN$^-$, bpy)	1.959	1.955	2.020
Fe-L4 (CN$^-$, bpy)	1.989	1.977	1.996
Fe-L5 (bpy)	1.992	1.959	2.020
Fe-L6 (bpy)	1.992	1.963	1.998

[a] Coordination site labeling corresponds with Figure 3.

The simulated absorption spectra for dyes **1**−**3** are shown in Figure 4. All three complexes display two absorption bands in the visible region. Excitations A−C (complex **1**) and A−F (complex **2**) can be all described as MLCT transitions. While the majority of the transitions A−J (complex **3**) also have a MLCT character, several transitions (D, E) have significant MC character.

Relevant particle states involved in the visible light transitions are shown in Figure 5, classified by the absorption band. Note that functionalization of the bipyridine ligand of dye **1** with dicarboxylic acid, resulting in dye **2**, changes the energetic ordering of the LUMO+1 and LUMO+2 orbitals. Complex **3** possesses two sets of degenerate of virtual orbitals (LUMO, LUMO+1, and LUMO+2, LUMO+3) and a contribution from the MC ligand field state (LUMO+12). The particle states shown in Figure 5 serve as initial (donor) states for the IET simulations reported below.

3.2. Dye-Nanoparticle Assemblies.

The linker models used to attach the dye molecules to the TiO$_2$ surface are shown in Figure 6. We have explored the cyanide attachment mode, and monodentate and bidentate attachment modes for carboxylic acid. Although multiple carboxylic acid binding modes exist, only two attachment modes are explored in this work, based on previously published stability analysis.[51]

3.2.1. Nonequivalent Dye Attachments. Each of the Fe(II) polypyridine compounds investigated can attach to the surface in multiple ways. Complex **3** can be anchored to the TiO$_2$ surface via a −COOH group attached at 4 or 4′ site of the bpy ligand. Similarly, two nonequivalent CN$^-$ sites for attachment are present in **1** and **2**. This results in two possible attachments of all three dyes onto the surface, in which the bipyridine group not bound to the surface is oriented either parallel or perpendicular relative to the (101) plane of TiO$_2$ (see Figure 7).

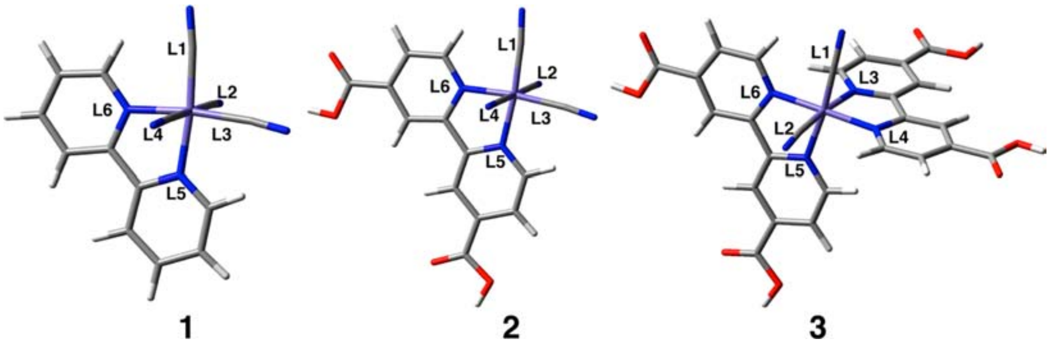

Figure 3. Optimized structures of dyes **1**, **2**, and **3** with each coordination site labeled (L1−L6).

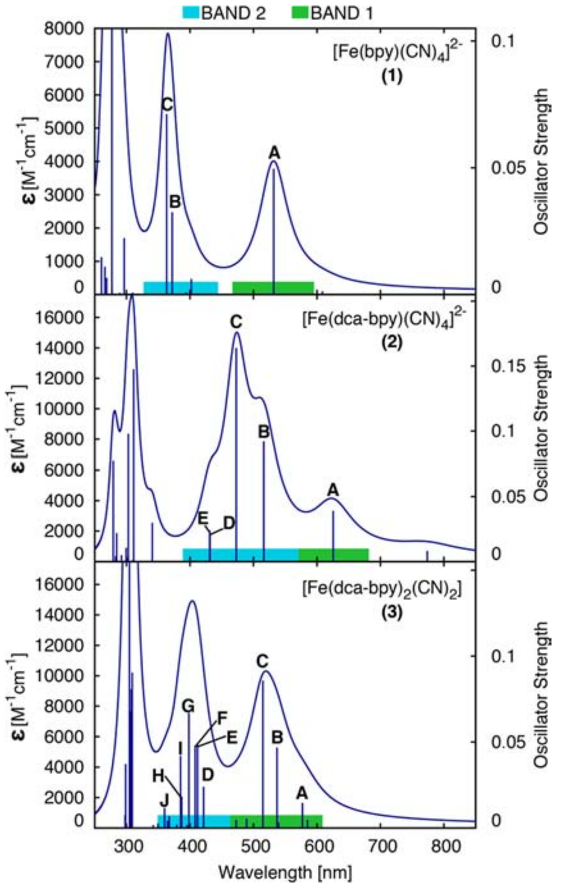

Figure 4. Simulated absorption spectra for (from top to bottom) dyes **1**, **2**, and **3** with Lorentzian broadening of HWMH = 0.12 eV with important excitations (f_{osc} > 0.01) in the visible region labeled, calculated with B3LYP TD-DFT in acetonitrile (PCM).

Dyes anchored to the surface via the CN$^-$ group have a free degree of rotation about the axis defined by the cyanide bond (see Figure 8). This ambiguity is caused by the fact that the HCN/TiO$_2$ surface model was chosen to model the full dye/TiO$_2$ assembly because of the computational constraints. A conformation that places the bipyridine groups as far from the surface as possible was chosen for the IET simulations reported here. This allows us to study the IET via the surface-anchoring group, rather than indirect IET between the bpy ligand group and TiO$_2$ surface because of their spatial proximity. The results of IET simulations with different orientations of the dyes on the surface are reported in the Supporting Information.

It is important to note that the structure optimization of the HCN/TiO$_2$ system (see Figure 8) resulted in a significantly longer N−Ti bond length (2.33 Å) than that reported by Selloni[52] (2.12 Å). Selloni and co-workers have optimized [Fe(CN)$_6$]$^{4-}$ on a Ti$_{38}$O$_{76}$ cluster, which likely provides a better model for this attachment. The influence of the N−Ti distance on the results on the IET rates was therefore investigated by setting the N−Ti bond length to 2.12, 2.22, and 2.33 Å in the IET simulations as shown in Figure 8.

3.3. IET Simulations.

Density of states plots for chromophore/nanoparticle assemblies calculated with the EH method are shown in Figures 9 and 10. For all three complexes investigated, dyes introduce occupied energy levels into the semiconductor band gap and a number of virtual energy levels (LUMO−LUMO+12 for dye **1**, LUMO−LUMO+13 for dye **2**, and LUMO−LUMO+15 for dye **3**) that couple with the conduction band of TiO$_2$.

Differences in the orbital energy levels among the three dyes are illustrated in Figure 10. Addition of carboxylic acid groups to bipyridine ligand of dye **1**, creating dye **2**, results in significant lowering of the orbital energies of LUMO−LUMO+2 states. Replacement of the two CN$^-$ ligands in dye **2** by an additional bipyridine ligand creating dye **3** results in three sets of doubly degenerate virtual orbitals (LUMO−LUMO+5).

Results of the IET simulations are summarized in Figures 11−13. In order for the IET to be competitive with the ultrafast intersystem crossing into a low-lying ^{5}T state in these complexes, the IET characteristic time, τ, should be smaller or equal to 100 fs.[18,20,21] A horizontal red line in Figures 11−13 denotes the characteristic time τ of 100 fs. Therefore, only the initial states with this or faster rates (i.e., lying below the red

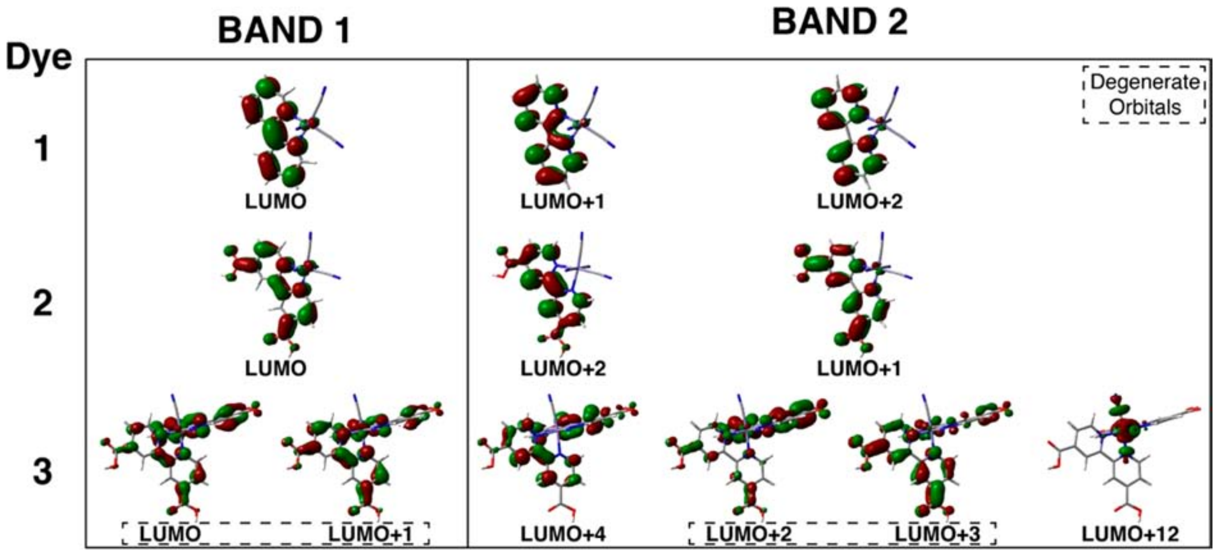

Figure 5. Relevant particle states for the major excitations (f_{osc} > 0.01) from the calculated spectra shown in Figure 4. Kohn−Sham orbitals are classified by the absorption band (columns) and by dye (rows).

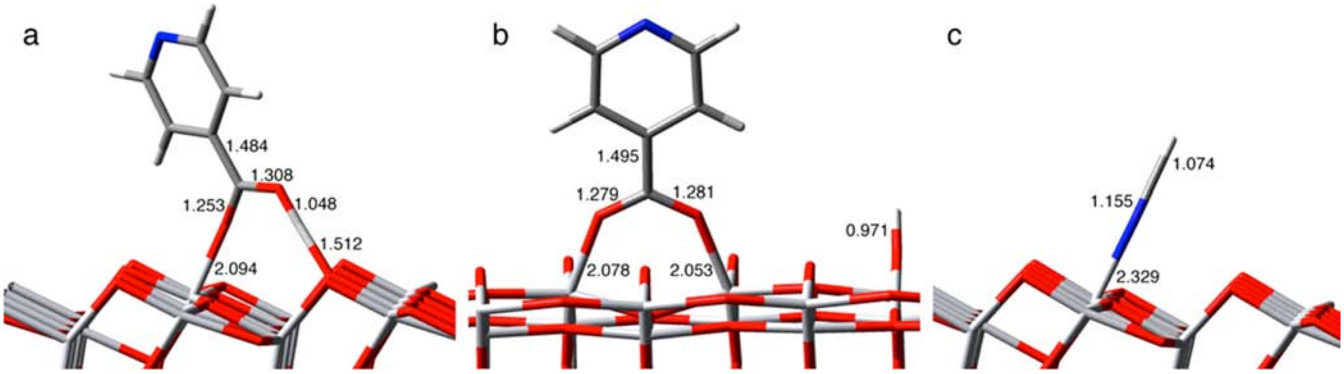

Figure 6. Optimized structures of anatase (101) with pyridine-4-carboxylic acid binding via a monodentate (a) and bidentate (b) binding mode, and hydrogen cyanide (c).

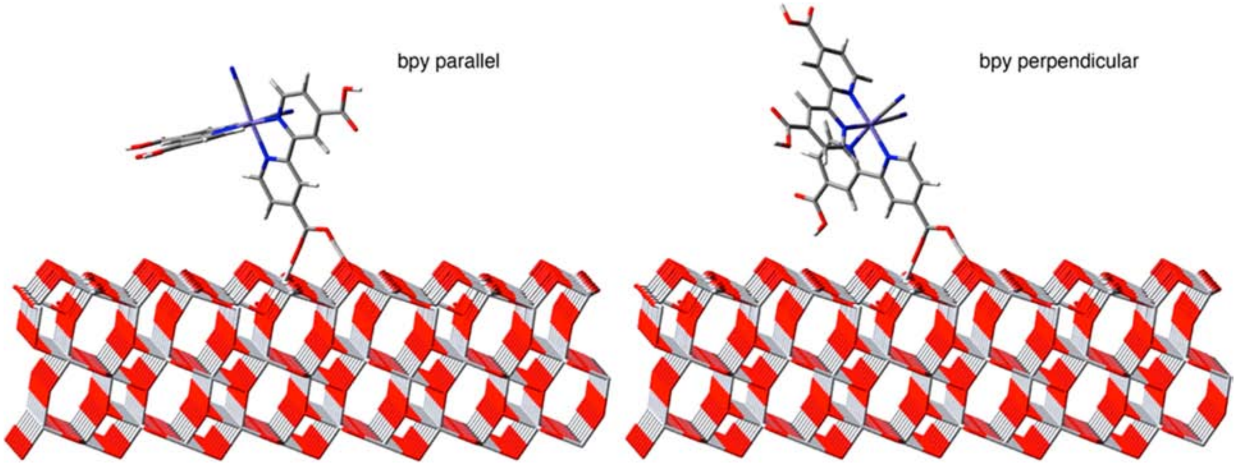

Figure 7. Final slab models of dye-nanoparticle assemblies consisting of [Fe(bpy-dca)$_2$(CN)$_2$] attached to anatase (101) via a monodentate carboxylic acid binding mode in the following nonequivalent orientations: bpy parallel (left) and bpy perpendicular (right).

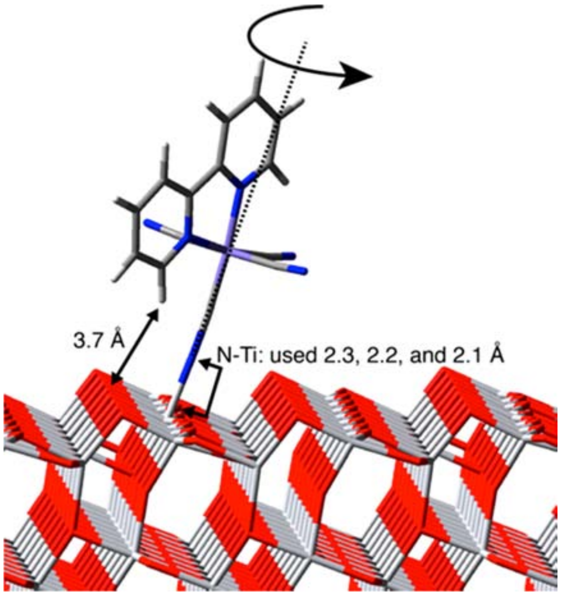

Figure 8. Structure of **1**-TiO$_2$ assembly employing CN$^-$ as the anchoring group.

line) will be capable of the electron injection into the TiO$_2$ semiconductor.

As can be seen in Figure 11, excited dye **1** will not undergo IET efficiently, as the majority of the characteristic times are between 483.0 fs and 17.7 ps. The only exception is the IET from the LUMO+1 orbital in the bpy perpendicular attachment. In the LUMO+1 case the characteristic times range between 137.3−101.6 fs, suggesting that while the IET is not very efficient in **1**-TiO$_2$ assemblies, it does occur for certain excitations. This is consistent with the work of Meyer[16] which indicates that the excited state charge transfer in **1**-TiO$_2$ assemblies occurs via a combination of the direct sensitization mechanism (i.e., direct charge-transfer excitation between the dye and the semiconductor) as well as the indirect mechanism (i.e., IET). It is also interesting to note that the IET is overall more efficient when the plane defined by the single bipyridine ligand is oriented perpendicular with respect to the TiO$_2$ surface. Additionally, variation of the CN$^-$ group distance from the TiO$_2$ surface between 2.12−2.33 Å does not significantly impact the calculated IET rates. Therefore, only Ti−N distance of 2.33 Å was considered in all subsequent IET simulations.

Figure 12 summarizes the IET rates for **2**-TiO$_2$ assemblies. Both bidentate and monodentate attachments via the carboxylic acid anchoring group were investigated, as well as the attachment via the CN$^-$ ligand. There are several conclusions that can be drawn from these results. First, IET via the CN$^-$ ligand for **2**-TiO$_2$ assemblies is much less efficient than in the case of the **1**-TiO$_2$. This is likely due to the stabilization of the

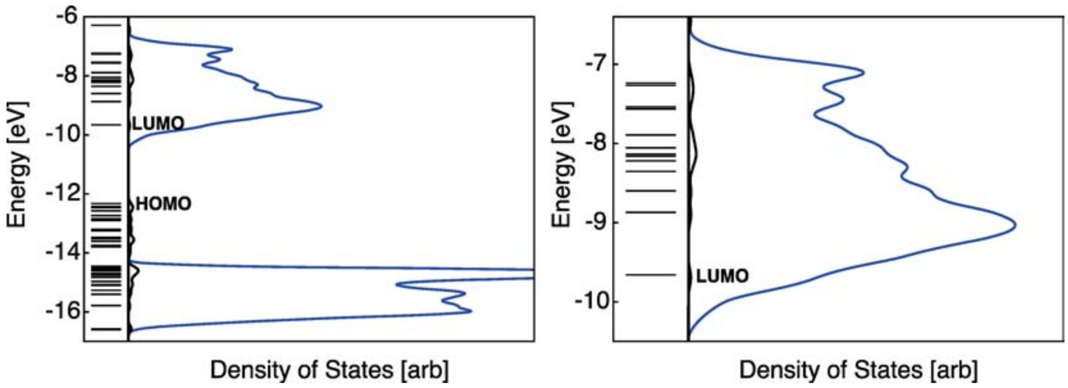

Figure 9. Density of states for **1**-TiO_2 anatase (101) slab model (left) and enlarged conduction band (right) show the following: total density of states (blue line), projected density of states on the dye (black line), and the energy levels of the dye in vacuum using EH (black level set lines). Gaussian line-shape (HWHM = 0.05 eV) used for convolution.

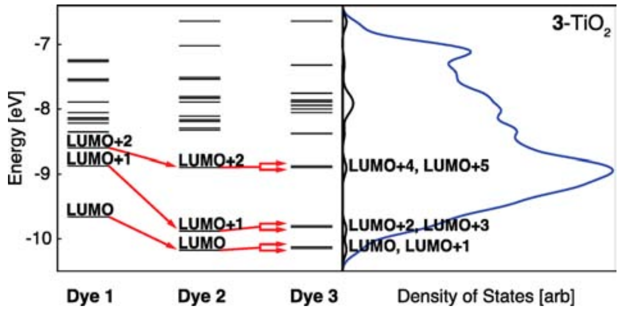

Figure 10. Discrete energy levels of the dyes (left) in vacuum, using EH level of theory, showing the evolution of the similar molecular orbitals, going from the smallest to the largest dye. The DOS/pDOS for the $[Fe(bpy\text{-}dca)_2(CN)_2]/TiO_2$ nanoparticle system is shown for reference (right, for full DOS/pDOS plot see Supporting Information).

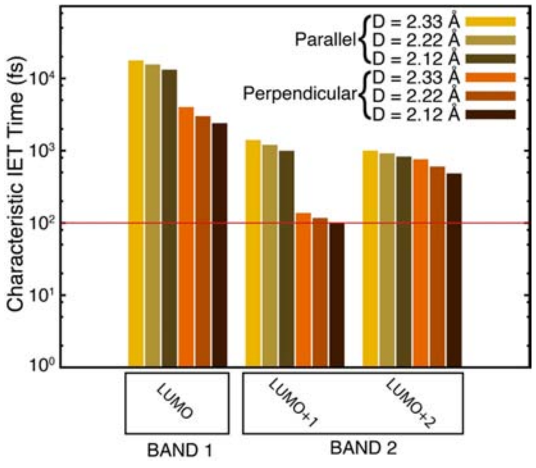

Figure 11. Characteristic IET times for relevant particle states of $[Fe(bpy)(CN)_4]^{2-}$ attached to the anatase (101) slab in both the “bpy parallel” and “bpy perpendicular” orientations via monodentate cyanide anchoring groups with varying nitrogen titanium distances (2.33, 2.22, and 2.12 Å), determined by exponential fitting.

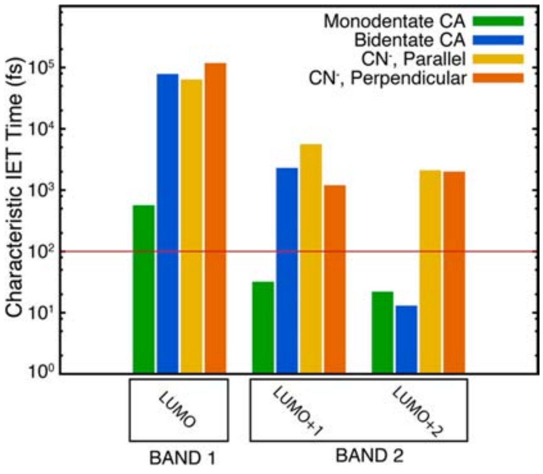

Figure 12. Characteristic IET times for relevant particle states of $[Fe(bpy\text{-}dca)(CN)_4]^{2-}$ attached to the anatase (101) slab by monodentate carboxylic acid, bidentate carboxylic acid, and cyanide anchoring groups (in both the “bpy parallel” and “bpy perpendicular” orientations), determined by exponential fitting.

MLCT states localized on the bpy ligand caused by addition of the carboxylic acid groups (see Figure 10). As a result, IET via the CN^- anchoring group will not be competitive with the ultrafast intersystem crossing events in these complexes. Second, this complex displays a band-selective IET when attached to the TiO_2 via the carboxylic acid anchoring group in both monodentate and bidentate binding modes. Interestingly, IET via the monodentate binding mode is overall more efficient than via the bindentate binding mode. Finally, comparison of the IET characteristic times among **1**-TiO_2 and **2**-TiO_2 leads us to conclude that indirect sensitization will be more efficient in **2**-TiO_2 thanks to the presence of the carboxylic acid anchoring groups. On the other hand, attachment of this complex via the carboxylic acid group will eliminate the direct sensitization mechanism that occurs when the complex is attached to TiO_2 via the CN^- group.[16]

Characteristic IET times for **3**-TiO_2 assemblies are shown in Figure 13. As can be seen in Figure 13, dye **3** undergoes a band-selective IET for all attachments investigated. Interestingly, attachment via the carboxylic acid anchoring group in monodentate binding modes results in the fastest IET rates on average. Note that while LUMO−LUMO+4 belong to the π^* ligand-localized states, LUMO+15 (which matches Kohn−Sham orbital LUMO+12) corresponds to a MC state (see Figure 5). This accounts for an ultrafast IET from this state (τ = 12.4 fs) for CN^- attachment, while significantly slower IET rates (τ = 302.9 fs to 7.3 ps) were observed for the **3**-TiO_2 assemblies employing carboxylic acid as the anchoring group.

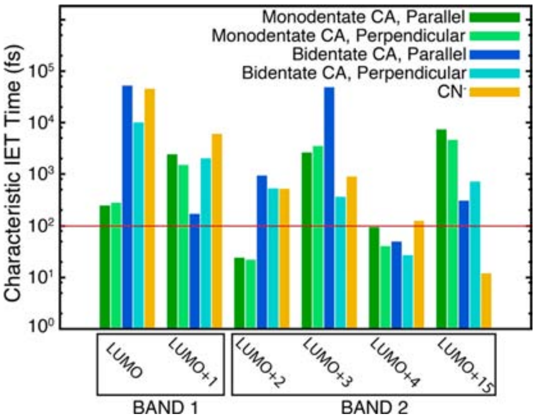

Figure 13. Characteristic IET times for relevant particle states of [Fe(bpy-dca)$_2$(CN)$_2$] attached to the anatase (101) slab by monodentate carboxylic acid (in both the "bpy parallel" and "bpy perpendicular" orientations), bidentate carboxylic acid (in both the "bpy parallel" and "bpy perpendicular" orientations), and cyanide anchoring groups, determined by exponential fitting.

Interestingly, band-selective indirect sensitization was observed in dye-TiO$_2$ assemblies for all three dyes investigated. While our results do not elucidate this phenomenon for the **1**-TiO$_2$ system, they do provide an explanation in case of the **2**-TiO$_2$ and **3**-TiO$_2$ assemblies. Band 1 (the lowest energy band in the UV−vis spectrum) corresponds to the excitations into the LUMO of **2** and a nearly degenerate set of LUMO and LUMO+1 orbitals of **3** (see Figures 4 and 5). These orbitals lie at the edge of the TiO$_2$ conduction band (see Figure 10) where the density of TiO$_2$ states is low, which results in (1) a small number of TiO$_2$ acceptor states available to couple with the donor states (LUMO, LUMO+1) of **2** and **3** and (2) a small driving force for the IET. Our results are consistent with the experimental observations of Ferrere and coworkers who first identified this band-selective behavior in **3**-TiO$_2$ assemblies.[14] Moreover, they also provide a pathway to improving the efficiency of these chromophores: To improve the IET efficiency, one needs to increase the energy of the LUMO and LUMO+1 states which should increase the driving force for the electron injection as well as provide a larger number of the TiO$_2$ acceptor states capable of coupling with the dye donor states. This could be, for example, achieved by targeted functionalization of their polypyridine scaffolds by electron donating groups, such as ethoxy, hydroxyl, or dimethylamino groups.[53]

It is important to note that according to the work of Meyer and co-workers, semiconductor sensitization in **1**-TiO$_2$ occurs by a combination of both direct and indirect sensitization mechanisms.[16] Moreover, according to their experimental studies, **1**-TiO$_2$ does not display band-selective sensitization. Direct sensitization is characterized by an electron being excited directly from the d^6 iron center into the Ti(IV) sites on the TiO$_2$. It is observed for dyes attached to TiO$_2$ via the CN$^-$ linkers.[54,55] Indirect sensitization occurs via the IET mechanism and can be observed for both CN$^-$ and carboxylic acid attachment modes. Computational studies presented here focus only on the indirect sensitization pathway and are thus not able to shed light on the efficiency of the direct sensitization in these assemblies. Our results, however, suggest that indirect sensitization becomes more important at higher excitation energies because of the long characteristic IET times displayed in the lower energy region (see Figure 11). Direct sensitization likely dominates the semiconductor sensitization mechanism in **1**-TiO$_2$ at lower energies.

In contrast to dye **1**, dye **3** attaches to the surface of TiO$_2$ exclusively via the carboxylic acid.[12] Therefore, in **3**-TiO$_2$, sensitization of the semiconductor surface is dominated by IET and our simulations are able to provide a reliable description of the band selective sensitization in these assemblies.

4. CONCLUSIONS

In this work we study initial excitation and subsequent IET among three Fe(II)-polypyridine dyes and TiO$_2$ anatase semiconductor. We find that all three complexes investigated can undergo IET at a time scale competitive with the ultrafast intersystem crossing of the initially excited ^{1}MLCT states into the low-lying MC states of higher multiplicities. The indirect sensitization is more efficient when the dyes are attached to the surface via the carboxylic acid anchoring group rather than CN$^-$. Attachment via the carboxylic acid in a monodentate binding mode also results in more efficient IET rates in comparison with the bidentate attachment.

The **3**-TiO$_2$ assembly displays band-selective sensitization, which is consistent with previous experimental findings by Ferrere and co-workers.[12,14] The origin of the band-selective behavior is attributed to the poor alignment of the lowest energy excited states with the conduction band of the TiO$_2$ semiconductor. This results in a poor driving force for the injection and insufficient density of the semiconductor acceptor states available for coupling with the dye donor states. One way to improve the efficiency of Fe(II)-polypyridine based dyes would be to increase the energy of their LUMO and LUMO+1 states with respect to the conduction band of the semiconductor. This could be, for example, achieved by targeted functionalization of their polypyridine scaffolds by electron donating groups.

■ ASSOCIATED CONTENT

Ⓢ Supporting Information

Diagrams of all dye-nanoparticle assembly structures, detailed summary of TD-DFT calculations (excitation wavelength, oscillator strength, Kohn−Sham orbitals involved), EH orbitals corresponding to relevant particle states, all DOS/pDOS plots, plots of survival probabilities over time for all simulations, and characteristic injection times based on constrained single and biexponential fits. This material is available free of charge via the Internet at http://pubs.acs.org.

■ AUTHOR INFORMATION

Corresponding Author

*E-mail: ejakubi@ncsu.edu.

Notes

The authors declare no competing financial interest.

■ ACKNOWLEDGMENTS

This research was supported by the Army Research Office Grant 59842-CH-II. We gratefully acknowledge Prof. Victor S. Batista and Dr. Robert Snoeberger III (Yale University) for providing us with a copy of the code for the IET simulations (IETsim) and for helpful discussions. D.N.B. also acknowledges support from the U.S. Department Of Education Graduate Assistantship In Areas Of National Need (GAANN) Fellowship Program at North Carolina State University.

■ REFERENCES

(1) Grätzel, M. *Inorg. Chem.* **2005**, *44*, 6841−6851.

(2) Hagberg, D. P.; Yum, J. H.; Lee, H. J.; De Angelis, F.; Marinado, T.; Karlsson, K. M.; Humphry-Baker, R.; Sun, L.; Hagfeldt, A.; Grätzel, M.; et al. *J. Am. Chem. Soc.* **2008**, *130*, 6259−6266.

(3) Hagfeldt, A.; Grätzel, M. *Acc. Chem. Res.* **2000**, *33*, 269−277.

(4) Polo, A. S.; Itokazu, M. K.; Murakami Iha, N. Y. *Coord. Chem. Rev.* **2004**, *248*, 1343−1361.

(5) Zhang, M. A.; Chen, C. C.; Ma, W. H.; Zhao, J. C. *Angew. Chem., Int. Ed.* **2008**, *47*, 9730−9733.

(6) Bae, E.; Choi, W. *Environ. Sci. Technol.* **2003**, *37*, 147−152.

(7) Abe, R.; Sayama, K.; Arakawa, H. *J. Photochem. Photobiol. A* **2004**, *166*, 115−122.

(8) Yella, A.; Lee, H. W.; Tsao, H. N.; Yi, C. Y.; Chandiran, A. K.; Nazeeruddin, M. K.; Diau, E. W. G.; Yeh, C. Y.; Zakeeruddin, S. M.; Gratzel, M. *Science* **2011**, *334*, 629−634.

(9) Nazeeruddin, M. K.; De Angelis, F.; Fantacci, S.; Selloni, A.; Viscardi, G.; Liska, P.; Ito, S.; Takeru, B.; Grätzel, M. *J. Am. Chem. Soc.* **2005**, *127*, 16835−16847.

(10) Ardo, S.; Meyer, G. J. *Chem. Soc. Rev.* **2009**, *38*, 115−164.

(11) Nazeeruddin, M. K.; Péchy, P.; Grätzel, M. *Chem. Commun.* **1997**, 1705−1706.

(12) Ferrere, S. *Chem. Mater.* **2000**, *12*, 1083−1089.

(13) Ferrere, S. *Inorg. Chim. Acta* **2002**, *329*, 79−92.

(14) Ferrere, S.; Gregg, B. A. *J. Am. Chem. Soc.* **1998**, *2*, 843−844.

(15) Yang, M.; Thompson, D. W.; Meyer, G. J. *Inorg. Chem.* **2002**, *41*, 1254−1262.

(16) Yang, M.; Thompson, D. W.; Meyer, G. J. *Inorg. Chem.* **2000**, *39*, 3738−3739.

(17) Xia, H. L.; Ardo, S.; Narducci Sarjeant, A. A.; Huang, S.; Meyer, G. J. *Langmuir* **2009**, *25*, 13641−13652.

(18) Monat, J. E.; McCusker, J. K. *J. Am. Chem. Soc.* **2000**, *122*, 4092−4097.

(19) Huse, N.; Cho, H.; Hong, K.; Jamula, L.; de Groot, F. M. F; Kim, T. K.; McCusker, J. K.; Schoenlein, R. W. *J. Phys. Chem. Lett.* **2011**, *2*, 880−884.

(20) Juban, E. A.; Smeigh, A. L.; Monat, J. E.; McCusker, J. K. *Coord. Chem. Rev.* **2006**, *250*, 1783−1791.

(21) Smeigh, A. L.; Creelman, M.; Mathies, R. a.; McCusker, J. K. *J. Am. Chem. Soc.* **2008**, *130*, 14105−14107.

(22) Becke, A. D. *J. Chem. Phys.* **1993**, *98*, 5648−5652.

(23) Stephens, P.; Devlin, F. *J. Phys. Chem.* **1994**, *98*, 11623−11627.

(24) Bowman, D. N.; Jakubikova, E. *Inorg. Chem.* **2012**, *51*, 6011−6019.

(25) Laurent, A. D.; Jacquemin, D. *Int. J. Quantum Chem.* **2013**, DOI: 10.1002/qua.24438.

(26) Dolg, M.; Wedig, U.; Stoll, H.; Preuss, H. *J. Chem. Phys.* **1987**, *86*, 866−872.

(27) Krishnan, R.; Binkley, J. S.; Seeger, R.; Pople, J. A. *J. Chem. Phys.* **1980**, *72*, 650−654.

(28) Clark, T.; Chandrasekhar, J.; Spitznagel, G. W.; Schleyer, P. V. R. *J. Comput. Chem.* **1983**, *4*, 294−301.

(29) Stratmann, R. E.; Scuseria, G. E.; Frisch, M. J. *J. Chem. Phys.* **1998**, *109*, 8218−8224.

(30) Casida, M. E.; Jamorski, C.; Casida, K. C.; Salahub, D. R. *J. Chem. Phys.* **1998**, *108*, 4439−4449.

(31) Bauernschmitt, R.; Ahlrichs, R. *Chem. Phys. Lett.* **1996**, *256*, 454−464.

(32) Scalmani, G.; Frisch, M. J. *J. Chem. Phys.* **2010**, *132*, 114110.

(33) Frisch, M. J. Trucks, G. W.; Schlegel, H. B.; Scuseria, G. E.; Robb, M. A.; Cheeseman, J. R.; Scalmani, G.; Barone, V.; Mennucci, B.; Petersson, G. A.; Nakatsuji, H.; Caricato, M.; Li, X.; Hratchian, H. P.; Izmaylov, A. F.; Bloino, J.; Zheng, G.; Sonnenberg, J. L.; Hada, M.; Ehara, M.; Toyota, K.; Fukuda, R.; Hasegawa, J.; Ishida, M.; Nakajima, T.; Honda, Y.; Kitao, O.; Nakai, H.; Vreven, T.; Montgomery, J. A.; , Jr., Peralta, J. E.; Ogliaro, F.; Bearpark, M.; Heyd, J. J.; Brothers, E.; Kudin, K. N.; Staroverov, V. N.; Kobayashi, R.; Normand, J.; Raghavachari, K.; Rendell, A.; Burant, J. C.; Iyengar, S. S.; Tomasi, J.; Cossi, M.; Rega, N.; Millam, J. M.; Klene, M.; Knox, J. E.; Cross, J. B.; Bakken, V.; Adamo, C.; Jaramillo, J.; Gomperts, R.; Stratmann, R. E.; Yazyev, O.; Austin, A. J.; Cammi, R.; Pomelli, C.; Ochterski, J. W.; Martin, R. L.; Morokuma, K.; Zakrzewski, V. G.; Voth, G. A.; Salvador, P.; Dannenberg, J. J.; Dapprich, S.; Daniels, A. D.; Ö. Farkas, Foresman, J. B.; Ortiz, J. V.; Cioslowski, J.; Fox, D. J. *Gaussian 09*, Revision A.02; Gaussian, Inc.: Wallingford, CT, 2009.

(34) Kresse, G.; Furthmüller, J. *Comput. Mater. Sci.* **1996**, *6*, 15−50.

(35) Kresse, G.; Furthmüller, J. *Phys. Rev. B* **1996**, *54*, 11169−11186.

(36) Kresse, G.; Hafner, J. *Phys. Rev. B* **1993**, *47*, 558−561.

(37) Kresse, G.; Hafner, J. *Phys. Rev. B* **1994**, *49*, 14251−14269.

(38) Perdew, J.; Burke, K.; Ernzerhof, M. *Phys. Rev. Lett.* **1996**, *77*, 3865−3868.

(39) Perdew, J.; Burke, K.; Ernzerhof, M. *Phys. Rev. Lett.* **1997**, *78*, 1396.

(40) Blöchl, P. E. *Phys. Rev. B* **1994**, *50*, 17953−17979.

(41) Kresse, G.; Joubert, D. *Phys. Rev. B* **1999**, *59*, 1758−1775.

(42) Jensen, K. P.; Roos, B. O.; Ryde, U. *J. Chem. Phys.* **2007**, *126*, 014103−014114.

(43) Kabsch, W. *Acta Crystallogr., Sect. A* **1978**, *34*, 827−828.

(44) Rego, L. G. C.; Batista, V. S. *J. Am. Chem. Soc.* **2003**, *125*, 7989−7997.

(45) Abuabara, S. G.; Cady, C. W.; Baxter, J. B.; Schmuttenmaer, C. A.; Crabtree, R. H.; Brudvig, G. W.; Batista, V. S. *J. Phys. Chem. C* **2007**, *111*, 11982−11990.

(46) McNamara, W. R.; Snoeberger, R. C., III; Li, G.; Schleicher, J. M.; Cady, C. W.; Poyatos, M.; Schmuttenmaer, C. A.; Crabtree, R. H.; Brudvig, G. W.; Batista, V. S. *J. Am. Chem. Soc.* **2008**, *130*, 14329−14338.

(47) Abuabara, S. G.; Rego, L. G. C.; Batista, V. S. *J. Am. Chem. Soc.* **2005**, *127*, 18234−18242.

(48) Jakubikova, E.; Snoeberger, R. C., III; Batista, V. S.; Martin, R. L.; Batista, E. R. *J. Phys. Chem. A* **2009**, *113*, 12532−12540.

(49) Nieuwenhuyzen, M.; Bertram, B.; Gallagher, J.; Vos, J. *Acta Crystallogr., Sect. C* **1998**, *54*, 603−606.

(50) Ma, B. Q.; Sun, H. L.; Gao, S. *Eur. J. Inorg. Chem.* **2005**, 3902−3906.

(51) Persson, P.; Lunell, S. *Sol. Energy Mater. Sol. Cells* **2000**, *63*, 139−148.

(52) De Angelis, F.; Tilocca, A.; Selloni, A. *J. Am. Chem. Soc.* **2004**, *126*, 15024−15025.

(53) Maestri, M.; Armaroli, N.; Balzani, V.; Constable, E. C.; Cargill Thompson, A. M. W. *Inorg. Chem.* **1995**, *34*, 2759−2767.

(54) Vrachnou, E.; Gratzel, M.; McEvoy, A. J. *J. Electroanal. Chem. Interfacial Electrochem.* **1989**, *258*, 193−205.

(55) Vrachnou, E.; Vlachopoulos, N.; Gratzel, M. *J. Chem. Soc., Chem. Commun.* **1987**, *0*, 868−870.